Petroleum Science 23 (2026) 4132–4144

Contents lists available at ScienceDirect

Petroleum Science

journal homepage: www.keaipublishing.com/en/journals/petroleum-science

Original Paper

Staged propagation mechanisms and their implications for fracture interaction and fracture swarm formation

Yao-Yang Li [a], Guang-Qing Zhang [a,b,*], Zhen-Yu Song [a]

[a] College of Petroleum Engineering, China University of Petroleum (Beijing), Beijing, 102249, China
[b] State Key Laboratory of Petroleum Resources and Engineering, China University of Petroleum (Beijing), Beijing, 102249, China

ARTICLE INFO

Article history:
Received 12 May 2026
Received in revised form
21 May 2026
Accepted 28 May 2026
Available online 3 June 2026

Edited by Meng-Jiao Zhou

Keywords:
Hydraulic fracturing
Fracture swarms
Fracture interference
Radial-circumferential fracture extension
Visualization experiments

ABSTRACT

Hydraulic fracture swarms are widely observed in post-fracturing core samples, yet their formation mechanisms remain incompletely understood. In this study, we employ a visualized experimental system to directly investigate their evolution using polymethyl methacrylate (PMMA) blocks. High-speed imaging is used to facilitate real-time observation and quantitative characterization of hydraulic fracture propagation under perturbed conditions. The results show that fracture growth follows a repeated cyclic three-stage sequence: (i) local nucleation, (ii) synchronously radial–circumferential propagation, and (iii) circumferentially dominated propagation. Stress shadowing promotes multi-point nucleation, whereas fluid-energy competition governs fracture-path selection among interacting fractures. When fracture-front velocity exceeds fluid-supply velocity, fluid-lag zones form near the tip, causing temporary arrest and subsequent re-nucleation. In the final stage, stress redistribution induces mixed Modes I–II propagation, generating step-like and shell-like fracture morphologies. The coupling between stress interference and fluid competition drives repeated propagation cycles, producing high-density fracture swarms consistent with field-core observations. These findings provide a physics-based framework for understanding the formation and evolution of hydraulic fracture swarm.

1. Introduction

With the rapid development of hydraulic fracturing technology, production from unconventional oil and gas reservoirs has increased significantly (Tahir et al., 2019; Song et al., 2025; Han et al., 2025). As horizontal well and multistage fracturing technologies continue to advance, unconventional reservoir exploitation is transitioning from single-layer development toward multilayer, three-dimensional reservoir stimulation (Lei et al., 2022). In this context, the propagation behavior and spatial distribution of induced fractures are critical for evaluating stimulation effectiveness and optimizing fracturing design.

Field coring campaigns conducted in North America and China have provided direct evidence of fracture geometries generated during hydraulic fracturing. Core observations from the Eagle Ford shale (Raterman et al., 2018), HFTS-1 (Wicker et al., 2018; Gale et al., 2019; Wang et al., 2019), and HFTS-2 (Maity et al., 2018; Gale et al., 2021; Han et al., 2023) consistently reveal dense fracture swarms aligned predominantly with the maximum horizontal stress, but with pronounced local deflections. Similar phenomena have been documented in the Qingcheng shale oil field (Zhang et al., 2024; Cao et al., 2025), tight conglomerate reservoirs in Xinjiang (Li et al., 2023), and the Fuling shale gas field (Song et al., 2024; Sun et al., 2025), where fracture counts within centimeter-scale core sections often exceed the number of perforations by several times (Fig. 1). These fractures commonly display branching, en-echelon patterns, and step-like or shell-like surface morphologies.

Despite the growing body of field evidence, a fundamental question remains unresolved: what underlying mechanism governs the systematic formation of hydraulic fracture swarms? Classical hydraulic fracturing theories, including the PKN, KGD, and penny-shaped models (Sneddon, 1946; Hubbert and Willis, 1957), predict continuous and symmetric bi-wing fracture growth perpendicular to the minimum horizontal principal stress. These models inherently assume stable propagation and therefore cannot explain the repeated fracture nucleation, localized arrest, or clustered spatial distributions observed in cores.

* Corresponding author.
E-mail address: zhangguangqing@cup.edu.cn (G.-Q. Zhang).
Peer review under the responsibility of China University of Petroleum (Beijing).

https://doi.org/10.1016/j.petsci.2026.05.054
1995-8226/

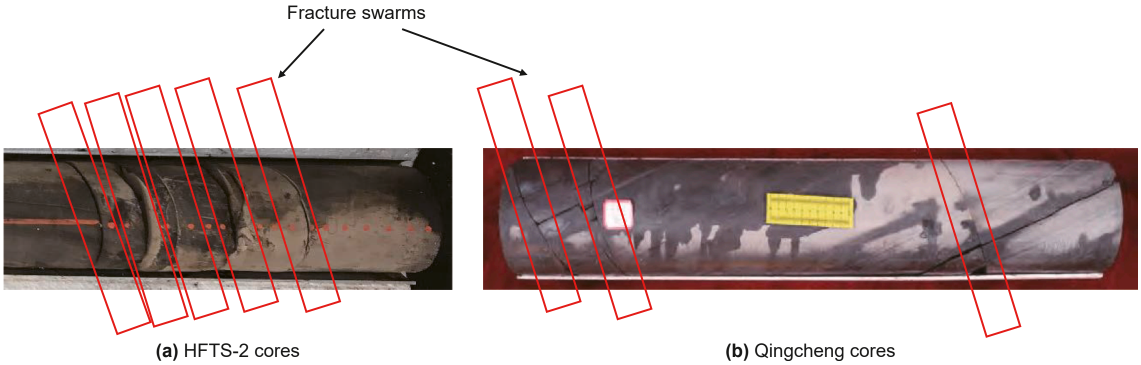

Fig. 1. Fracture morphology from hydraulic fracturing test sites.

Subsequent studies have suggested that fracture complexity may arise from geological and mechanical heterogeneity, including natural fractures (Hu et al., 2023), bedding planes (Dontsov and Suárez-Rivera, 2020; Abe et al., 2021; Tan et al., 20222), pore-pressure variations (AlTammar et al., 2018), rock anisotropy (Sakha et al., 2023), and lithological contrasts (He et al., 2016). Although these factors can locally modify fracture trajectories, they are reservoir-dependent and spatially stochastic. As such, they do not fully explain the repeatable and organized occurrence of high-density fracture swarms observed across different basins and stimulation scales.

Inter-fracture stress interference, commonly referred to as stress shadowing, has been recognized as a key mechanism influencing fracture morphology (Manríquez, 2018; Sobhaniaragh et al., 2018; Sobhaniaragh et al., 2019). Analytical and numerical studies have demonstrated that stress redistribution can promote fracture deflection, suppress propagation, or enhance network complexity. Advanced diagnostic techniques, including acoustic emission monitoring (Xing et al., 2019), CT and NMR imaging (Ishida et al., 1997; Talebi and Boone, 1998), and microseismic monitoring (Urbancic et al., 1999; Gale et al., 2018), have provided valuable insights into fracture geometries. However, these approaches primarily yield post-fracturing or indirect observations and rarely capture the dynamic evolution of interacting fractures.

Recent laboratory investigations have begun to reveal that fracture growth may involve local nucleation and rapid transverse crack-front expansion (Cochard et al., 2024), as well as alternating radial–circumferential propagation under interference conditions (Sun et al., 2024). These findings suggest that hydraulic fracture swarms may arise from intrinsic stage-dependent propagation dynamics rather than solely from external heterogeneity. Nevertheless, a unified mechanistic framework integrating stress interference, fluid transport, and cyclic fracture propagation under perturbed stress conditions remains lacking.

Therefore, the objective of this study is to experimentally investigate whether hydraulic fracture swarms can emerge from fracture propagation behavior governed by stress–fluid coupling. By employing a visualized hydraulic fracturing system that combines transparent PMMA specimens, controlled stress perturbation, and high-speed imaging, we quantitatively evaluate fracture propagation velocities, fluid-lag development, and inter-fracture interactions. Through a stage-dependent analysis of fracture nucleation, competition, and reactivation, we provide an explanation for the formation mechanism of hydraulic fracture swarms under coupled stress–fluid conditions.

2. Visualized fracturing experiments

At present, the understanding of hydraulic fracture propagation relies primarily on microseismic monitoring, post-fracturing coring, and numerical simulation. Microseismic techniques can partially reconstruct the spatial distribution of fractures; however, because these interpretations are derived from elastic wave responses associated with rock failure, they cannot directly resolve the transient propagation processes or the detailed evolution of fracture tips. Post-fracturing coring and imaging logs provide direct and reliable constraints on fracture geometry, yet they are inherently limited to static observations after stimulation and therefore fail to capture the dynamic evolution of fractures under perturbed conditions. Numerical simulations are widely used to analyze stress redistribution and fracture growth tendencies within fracture systems, but their predictive capability is strongly dependent on model assumptions and parameter selection, suggesting a lack of direct observational constraints. Consequently, conventional approaches remain insufficient for experimentally capturing the dynamic processes of fracture propagation and for elucidating the mechanistic role of stress interference in fracture evolution.

2.1. Visualized experimental system for hydraulic fracturing

To meet the requirements for visualizing fracture perturbation processes, a visualized experimental system for hydraulic fracturing was designed and constructed in this study. The system comprises a fracturing apparatus, a constant-rate fluid injection unit, transparent specimens, and a high-speed imaging system. The fracturing apparatus is used to apply confining pressure, while the constant-rate injection unit enables stable injection of fracturing fluid under controlled flow-rate conditions. Custom-fabricated transparent specimens are employed to simulate fracture propagation under reservoir-relevant conditions. The high-speed imaging system, in conjunction with auxiliary lighting, ensures clear and reliable capture of fracture initiation and propagation processes.

Compared with conventional experimental approaches, the proposed system offers several distinct advantages. (1) Direct visualization of fracture propagation: A high-speed imaging system operating at 240 frames per second (fps) with a spatial resolution of 1920 × 1080 pixels continuously records the entire fracture propagation process, enabling direct observation of the influence of stress shadowing at different propagation stages and overcoming the limitations of microseismic techniques, which primarily resolve final fracture geometries. (2) Controllable perturbation intensity: By systematically adjusting well spacing and inter-fracture spacing, the intensity of fracture interaction can be precisely controlled, providing a robust experimental basis for investigating fracture propagation behavior under varying perturbation conditions. (3) Elimination of heterogeneity-induced interference: The high homogeneity of polymethyl methacrylate (PMMA) specimens effectively eliminates random influences associated with reservoir anisotropy and lithological heterogeneity, allowing the experiments to focus explicitly on the role of inter-fracture interactions in governing fracture growth. (4) Synchronized dual-perspective observation: Simultaneous acquisition of frontal and lateral views using dual high-speed cameras enables precise identification of differences in stress-interference mechanisms from multiple observational perspectives.

2.2. Experimental materials and similarity considerations

Polymethyl methacrylate (PMMA) was selected as the rock-analog material for the visualized hydraulic fracturing experiments. Owing to its excellent optical transparency and high degree of homogeneity, PMMA enables real-time observation of fracture propagation while effectively eliminating the influence of intrinsic rock heterogeneity at the experimental scale. This material choice allows the experiments to focus explicitly on the role of fracture-induced perturbations and inter-fracture interactions in governing fracture evolution. The fracture toughness of PMMA, together with those of representative unconventional reservoir rocks, is summarized in Table 1.

PMMA has been widely adopted as a rock-analog material in experimental studies of hydraulic fracturing. Its fracture toughness is comparable to that of typical unconventional reservoir rocks, providing a basis for investigating fracture initiation and propagation behavior. In addition, the brittle fracture characteristics of PMMA closely resemble those of reservoir rocks, further supporting its suitability for fracture-mechanics investigations.

It should be noted, however, that the elastic modulus of PMMA (3.24 GPa) is lower than that of typical reservoir rocks (20–40 GPa). This contrast leads to relatively larger fracture apertures under equivalent stress conditions. Nevertheless, this difference does not invalidate the investigation of inter-fracture interaction mechanisms. Under the framework of linear elastic fracture mechanics (LEFM), stress transmission, stress shadow formation, and stress intensity factor (SIF) redistribution are primarily governed by geometric configuration, elastic properties, and fracture spacing. Both PMMA and reservoir rocks behave as linear elastic brittle solids prior to fracture initiation, allowing the governing fracture mechanics principles to remain applicable under scaled laboratory conditions.

In the present study, stress similarity was implemented through geometric scaling and controlled external loading. A uniaxial compressive stress of 1.5 MPa was applied in the top-view direction to simulate the maximum horizontal principal stress in the reservoir. The remaining two orthogonal directions were left unconstrained to facilitate optical observation. Under these conditions, fracture propagation can be governed by differential stress. In addition, the use of uniaxial loading minimizes the interference caused by confining-pressure anisotropy and boundary-coupling effects, thereby allowing the fracture evolution behavior to be more clearly isolated and interpreted.

The use of homogeneous PMMA specimens intentionally removes lithological randomness, ensuring that fracture nucleation, temporary arrest, reactivation, and branching arise primarily from stress redistribution and fluid transport dynamics rather than from material heterogeneity. Therefore, the experimental results are not intended to replicate absolute reservoir-scale magnitudes, but to isolate and directly visualize intrinsic stress–fluid coupling mechanisms governing cyclic fracture propagation. In this sense, the experiments complement numerical simulations by providing dynamic validation of interacting fracture behavior under controlled perturbation conditions.

Fig. 2 shows the PMMA specimen prepared to simulate multistage hydraulic fracturing in a horizontal well under spatial stress disturbance. The dimensions of the PMMA specimen are 200 mm × 200 mm × 300 mm. Two through-holes with a diameter of 20 mm were drilled to accommodate the injection pipelines. The through-holes at position I and position II were treated by cutting two notches with a diameter of 26 mm to simulate pre-existing fractures. In Fig. 2, the black sealing rings fix the injection pipelines within the wellbore. The wellbore is fractured sequentially from right to left by moving the injection point along the wellbore, continuously altering the stress state inside the specimen. The three-view perspectives are indicated in Fig. 2(a).

The processed PMMA specimen illustrates the wellbore position and pre-fabricated kerfs used to initiate hydraulic fractures, together with the defined top, front, and side viewing directions for optical observation during the experiments. The sealing ring serves a function similar to that of a bridge plug.

The fracturing fluid used in the experiments was formulated from deionized water, a guar gum thickening agent, and a fluorescent tracer. Guar gum was added to regulate fluid viscosity, imparting pronounced non-Newtonian rheological behavior over a range of shear rates. The fluorescent tracer enhanced the optical visibility of the fracturing fluid within propagating fractures. At the experimental scale, this fluid system effectively captures the influence of viscosity variations on hydraulic fracture propagation behavior. Under ambient conditions, the fracturing fluid exhibits shear-thinning behavior, with apparent viscosity decreasing from approximately 50 mPa·s at low shear rates to around 15 mPa·s at elevated shear rates.

2.3. Experimental design and data analysis

2.3.1. Experimental parameter design

To investigate the mechanisms governing hydraulic fracture swarm propagation, the experimental parameters were designed around two key controlling factors: inter-fracture interaction intensity and fluid energy input. A constant uniaxial external stress of 1.5 MPa was applied to the specimen in the top-view direction using the visualized experimental system for hydraulic fracturing, thereby simulating the maximum horizontal principal stress in the reservoir. The remaining two orthogonal directions were left unconstrained to serve as optical observation windows for the high-speed imaging system.

Uniaxial loading was applied to maintain constant differential stress conditions and to isolate fracture–fracture interactions. Under fully triaxial stresses conditions, fracture interaction is expected to follow a similar pattern when the differential stress is maintained.

Table 1
Fracture toughness of PMMA and representative unconventional reservoir rocks (Sun et al., 2024).

Material	Fracture toughness, MPa·m$^{-0.5}$
PMMA	1.50
Longmaxi shale	1.13–1.38
Clashach sandstone	1.04
Ruhr sandstone	1.64

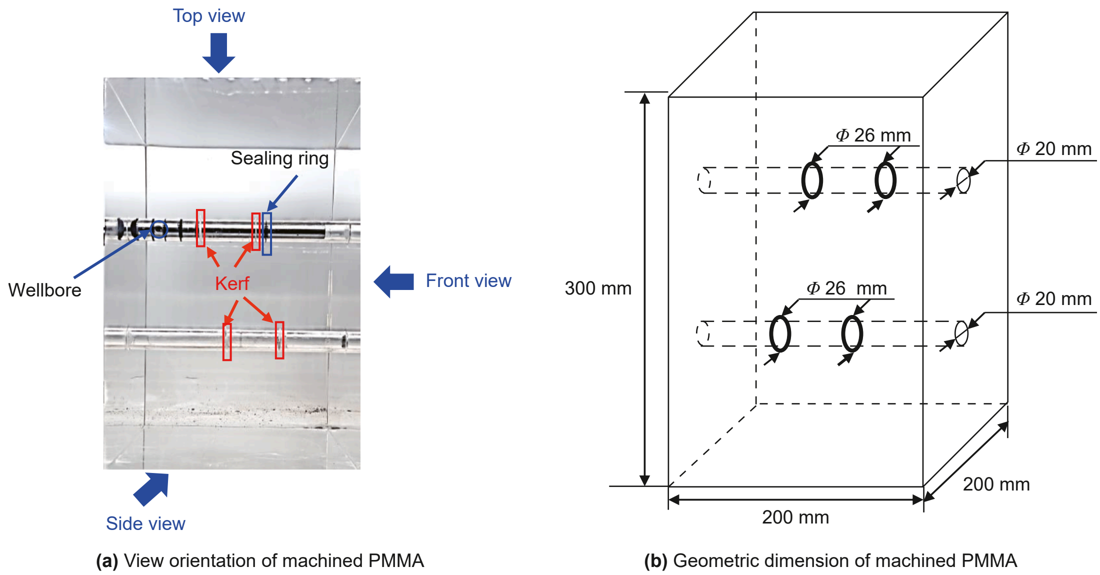

Fig. 2. The machined PMMA and view orientation.

By maintaining a single principal stress direction, the present design enables clear identification of stress-induced fracture deflection, branch nucleation, and stress intensity redistribution arising primarily from fracture interaction. This mechanism-isolating approach allows direct visualization of stage-dependent propagation behavior, which cannot be readily captured through post-fracturing diagnostics or indirect monitoring techniques.

Under these conditions, hydraulic fracture propagation behavior is jointly controlled by inter-fracture spacing and injection rate. Inter-fracture spacing is further regulated through the prescribed well spacing and inter-fracture spacing in the prefabricated specimens. In this study, systematic variations in well spacing and inter-fracture spacing were implemented to differentiate levels of inter-fracture interaction intensity, thereby enabling investigation of the effects of fracture interaction on fracture propagation behavior. The injection rate was used to characterize the level of fluid energy input, allowing comparative analysis of fracture propagation behavior under different fluid energy supply conditions.

The specific combinations of experimental parameters are summarized in Table 2. Specimens #1 and #2 were configured with different well spacing and inter-fracture spacing to compare hydraulic fracture propagation behavior under varying levels of inter-fracture interaction intensity. By contrast, specimens #1 and #3 were tested under identical inter-fracture interaction conditions but with different injection rates, allowing assessment of the influence of fluid energy input on stage-dependent fracture propagation characteristics and fracture competition behavior. To facilitate discrimination of individual fracture propagation paths, fracturing fluids containing fluorescent tracers of different colors were injected separately at different wellbore locations.

Table 2
Experimental parameter design.

Specimen ID	Well spacing, mm	Inter-fracture spacing, mm	Injection rate, mL/min
#1	100	5	30
#2	150	8	30
#3	100	5	45

2.3.2. Experimental procedure

The overall procedure of the visualized hydraulic fracturing experiments is illustrated in Fig. 3. Prior to testing, the processed PMMA specimen was securely mounted in the hydraulic fracturing apparatus, and the injection lines were connected and checked for sealing integrity. The prepared fracturing fluid was then loaded into the constant-rate injection system in preparation for the subsequent injection stage.

After the experiment commenced, the injection line was first connected to wellbore 1. Hydraulic fracturing was conducted sequentially in wellbores 1 and 2. Specifically, the red fracturing fluid was first injected at location I, followed by the injection of the blue fracturing fluid at location II. This sequential injection scheme allowed the investigation of fracture competition dynamics, with each fracture being influenced by the stress field created by the previous one. The sequential injection induced a dynamic interplay between fractures, as shown in Figs. 5 and 6. Simultaneously, the high-speed imaging system was activated to record fracture initiation and subsequent propagation. Upon completion of this experimental stage, the injection line was switched to wellbore 2, and the same procedure was repeated. To distinguish the

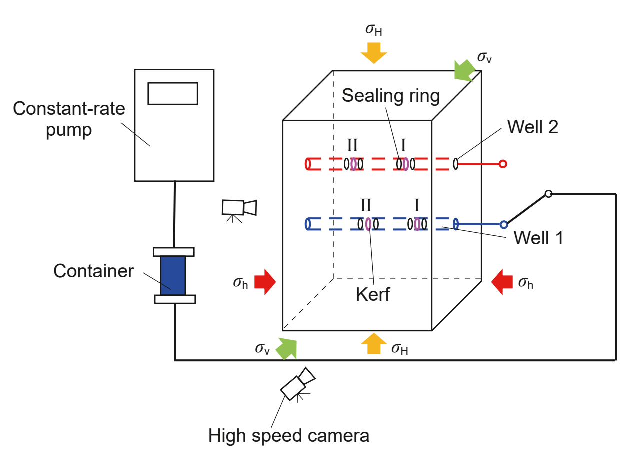

Fig. 3. Schematic of the visualized hydraulic fracturing experiment.

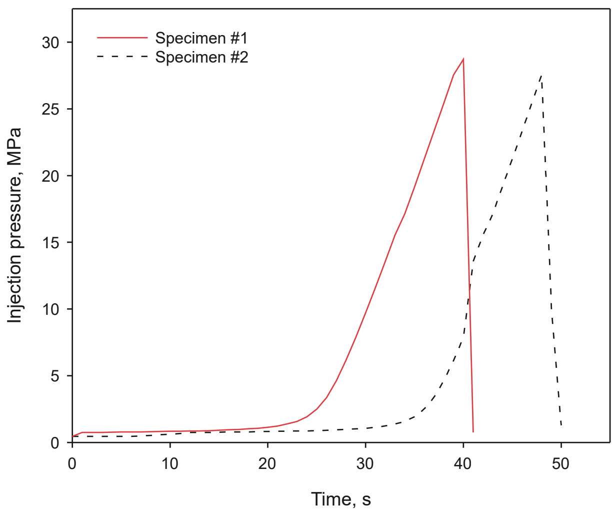

Fig. 4. Pump pressure–time curves during sequential hydraulic fracturing experiments.

propagation behavior of individual fractures, a red fracturing fluid was injected at location I, whereas a blue fracturing fluid was used at location II.

The fracturing fluid used in the experiments had a viscosity of 50 mPa·s. According to the similarity principle and relevant scaling laws, this fluid viscosity was chosen to be comparable to commonly used water-based fracturing fluids in field-scale applications. While the laboratory-scale fractures are much smaller than field-scale fractures, this viscosity allows for a reasonable representation of the fluid dynamics and fracture–fluid interaction involved in hydraulic fracturing. The fluid viscosity was selected to simulate the behavior of typical hydraulic fracturing fluids under field conditions, ensuring the results remain relevant to engineering applications.

Throughout the experiments, injection pressure and injection time were synchronously recorded, while the high-speed imaging system continuously acquired video data of fracture propagation. After completion of the experiments, the video recordings and pressure data were systematically processed and integrated to analyze the dynamic behavior of hydraulic fracture propagation.

The workflow illustrates specimen installation, application of uniaxial external stress, sequential constant-rate fluid injection at designated locations, synchronized high-speed imaging, and synchronous recording of injection pressure and time, followed by post-experimental data processing and analysis.

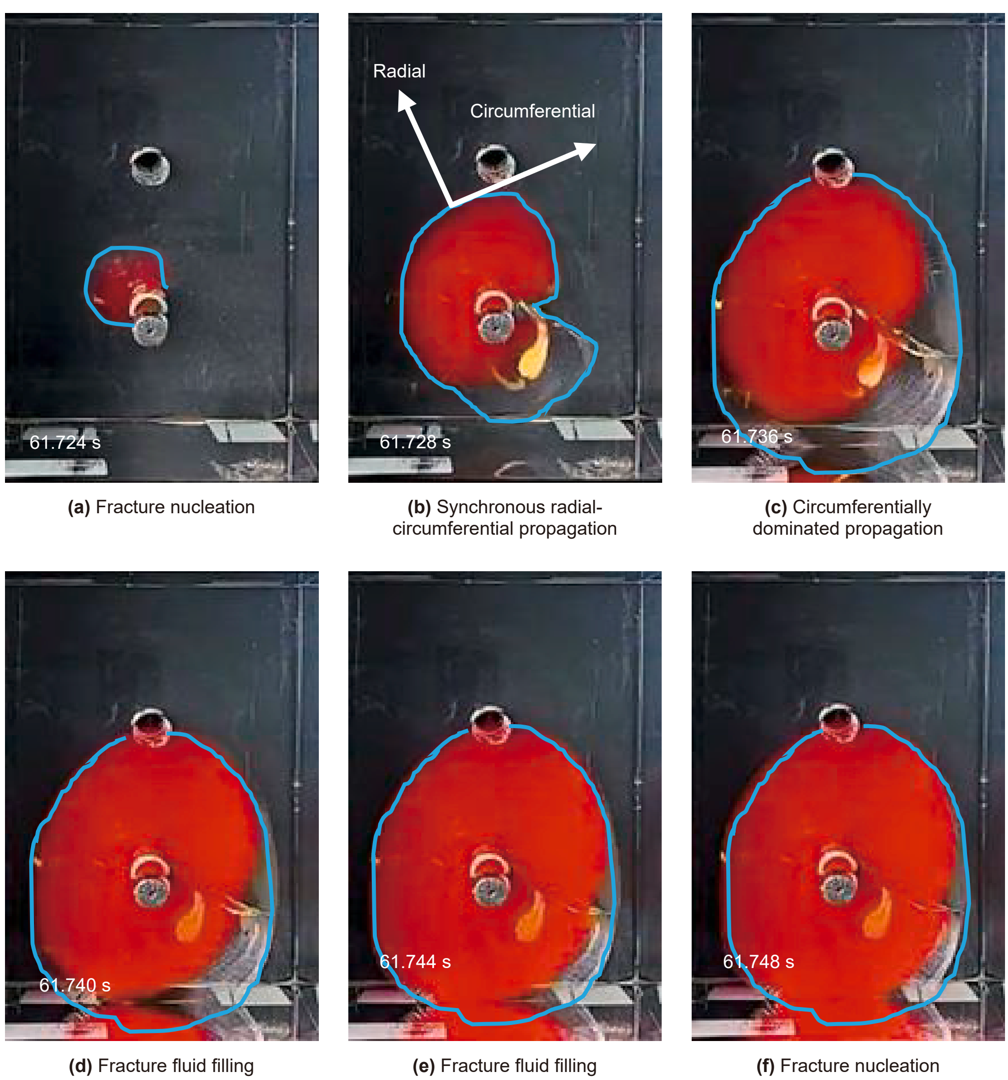

Fig. 5. Evolution of a single hydraulic fracture during one complete propagation cycle of specimen 2.

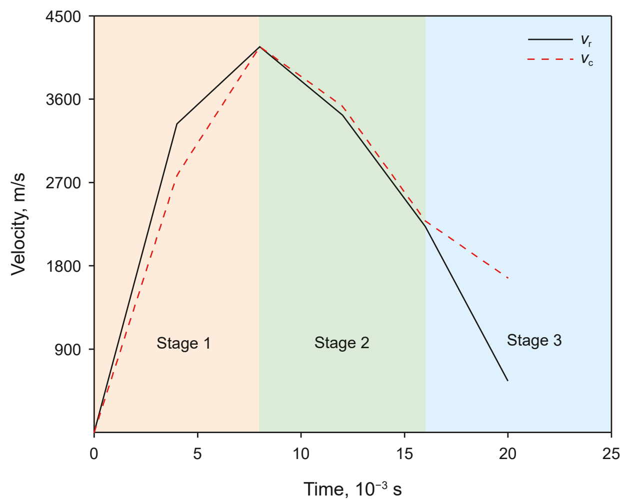

(a) Comparison of radial and circumferential fracture propagation velocities

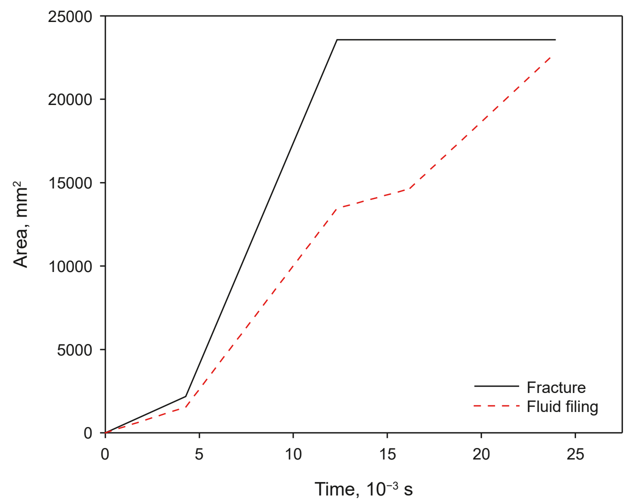

(b) Evolution of total fracture area and fracturing-fluid-filled area

Fig. 6. Quantitative characterization of stage-dependent hydraulic fracture propagation.

2.3.3. Data processing

Video data of the fracture propagation process were processed using digital image analysis techniques. First, the high-speed imaging recordings were decomposed into individual frames to extract image sequences corresponding to key stages of fracture propagation. Subsequently, quantitative identification of the fracture front and the fracturing-fluid-filled region was performed using the ImageJ image analysis platform. Semi-automated recognition of fracture outlines was achieved through grayscale thresholding and edge-detection methods, combined with manual correction to improve the accuracy of fracture-front localization.

Based on the identified fracture fronts, the temporal evolution of fracture extension distances in different directions was calculated, allowing determination of radial and circumferential fracture propagation velocities. In parallel, a comparative analysis between the fracturing-fluid-filled region and the fracture geometry was conducted to identify the formation and evolution of fluid-lag zones during fracture propagation.

To characterize the stage-dependent features of fracture propagation, the propagation process was segmented into distinct stages by integrating variations in fracture propagation velocity, the geometric evolution of fracture morphology, and the state of fracturing-fluid filling. By comparing the characteristics of fracture propagation stages under different experimental conditions, the effects of inter-fracture interaction intensity and fluid energy input on the dynamics of hydraulic fracture swarm propagation were systematically evaluated.

3. Cyclic three-stage propagation controlling hydraulic fracture swarm formation and evolution

3.1. Three-stage propagation sequence of hydraulic fracture swarms

3.1.1. Experimentally observed stage-dependent characteristics

In Fig. 4, the pump pressure–time responses during the hydraulic fracturing experiments are presented. For both wellbores, the pressure initially increased gradually due to fluid accumulation within the sealed system, followed by rapid fracture breakdown.

High-speed imaging clearly captured the morphological evolution of a single hydraulic fracture during the formation of a complete fracture surface, as shown in Fig. 5. The development of a fully formed hydraulic fracture surface proceeded through three distinct stages.

3.1.1.1. Stage I: fracture nucleation. Visualized experiments show that, during the initial stage of hydraulic fracture initiation, fracture nucleation occurred locally, forming discrete nucleation sites rather than an immediately continuous fracture surface. These locally nucleated fractures served as the precursors for subsequent large-scale fracture development (Fig. 5(a)).

3.1.1.2. Stage II: synchronous radial–circumferential propagation. With continued fluid injection, the fracture system transitioned into a stage characterized by synchronous radial and circumferential propagation (Fig. 5(b)). During this stage, fracture extension occurred simultaneously in both directions, leading to a rapid increase in fracture surface area, while the fracture-front propagation velocity reached its maximum. Notably, fracture growth was no longer confined to the direction perpendicular to the maximum horizontal principal stress. Instead, coupled radial–circumferential expansion dominated, and the fracture surface progressively evolved towards a symmetric penny-shaped fracture.

3.1.1.3. Stage III: circumferentially dominated propagation. Once the fracture reached a critical size, the radial propagation rate decreased markedly, and fracture growth progressively transitioned into a circumferentially dominated stage (Fig. 5(c)). During this stage, fracture extension was characterized by sustained circumferential advancement, whereas radial fracture-tip propagation became largely arrested. Concurrently, the fracture surface evolved from an initially asymmetric geometry towards a symmetric configuration, ultimately forming a fully developed fracture surface.

Following the formation of a complete fracture surface, continued fluid injection led to progressive filling of the entire fracture plane (Fig. 5(d) and (e)). Subsequently, the fracture surface came into contact with the lower boundary, resulting in complete pressure release within the fracture (Fig. 5(f)) and marking the onset of the next propagation cycle.

To quantitatively characterize the stage-dependent evolution of hydraulic fracture propagation, the growth behavior of an undisturbed single fracture was analyzed in detail, as shown in Fig. 6.

3.1.1.4. Stage I (0 – 0.008 s): fracture nucleation stage. During this stage, both radial and circumferential fracture propagation velocities increased rapidly from zero to a peak value of approximately 3.8 m/s. Concurrently, the ratio of radial to circumferential propagation velocity decreased rapidly, indicating the onset of directional differentiation in fracture growth. The fracture surface area increased from zero to approximately 2000 mm^2, while the ratio of fracture area to fracturing-fluid-filled area remained low. This stage corresponds to rapid fracture nucleation and played a critical role in determining the subsequent fracture propagation pathway.

3.1.1.5. Stage II (0.008 – 0.016 s): synchronous radial–circumferential propagation stage. During this stage, the ratio of radial to circumferential propagation velocity stabilized within the range of 0.9–1.1, indicating a dynamic balance between radial and circumferential fracture growth. The fracture surface area entered a quasi-linear growth regime. Notably, although the injection rate remained constant, fluctuations were observed in the fracturing-fluid filling rate (Fig. 6(b)). These fluctuations arose from geometric confinement imposed by the evolving fracture shape, which progressively redirected fluid transport from synchronous radial–circumferential flow toward circumferentially dominated flow, highlighting the strong control exerted by fracture geometry on fluid transport behavior.

3.1.1.6. Stage III (0.016–0.024 s): circumferentially dominated propagation stage. In this stage, the radial propagation velocity decreased rapidly, whereas the rate of reduction in circumferential propagation velocity slowed, causing the ratio of radial to circumferential velocity to decline progressively to approximately 0.3. Meanwhile, the fracturing-fluid filling rate recovered, indicating that fluid transport became predominantly circumferential as the fracture surface is progressively filled.

3.1.2. Physical mechanisms governing the three-stage fracture propagation

The three-stage fracture propagation behavior is jointly governed by fluid transport within the fracture and geometric boundary constraints imposed by the evolving fracture surface. Fluid flow inside the fracture can be described using lubrication theory, and the corresponding governing equation is given in Eq. (1):

$$\frac{\mathrm{d}p}{\mathrm{d}x} = -K\left(\frac{2n+1}{2n}q\right)^{n}\left(\frac{2}{w}\right)^{2n+1} \tag{1}$$

where p denotes the fluid pressure, x is the spatial coordinate along the fracture, K is the consistency index characterizing the effective fluid viscosity, n is the flow behavior index, w represents the fracture aperture, and q is the local volumetric fluid flux within the fracture.

Fluid pressure within the fracture varies along the fracture length and is jointly controlled by fluid viscosity, fracture aperture, and the effective flow pathways. When the fracture-front propagation velocity exceeds the capacity of fluid-supply capacity towards the fracture tip, a fluid-lag zone develops near the tip. This fluid lag reduces the effective driving pressure acting at the fracture front, thereby inducing temporary fracture arrest.

During Stage I (fracture nucleation), the fracture remains small in scale, resulting in short fluid-transport pathways and sufficient fluid-pressure supply at the fracture tip. Under these conditions, localized pressure concentration triggers the formation of fracture nuclei, leading to rapid fracture initiation, with close proximity between the fracture front and the fluid front. However, as the fracture-front propagation velocity progressively exceeds the capacity of fluid-supply capacity, fluid-lag effects rapidly emerge. Consequently, the energy available at the fracture tip decreases and eventually falls below the critical energy release rate, inducing temporary arrest of fracture propagation.

Geometric constraints imposed by the evolving fracture surface modify the distribution of fluid pressure within the fracture. Following fracture nucleation, newly formed local fracture surfaces provide preferential pathways for fluid transport. As fracture propagation proceeds, fluid flow is increasingly constrained by the in-situ stress field, causing the injected fluid to be redistributed into radial and circumferential flow components. When the fracture surface remains limited in extent, the available fluid energy is sufficient to sustain both radial and circumferential propagation. However, as the fluid-lag zone progressively expands, the available fluid energy becomes insufficient to support radial growth and is instead preferentially channeled into circumferential propagation. This redistribution results in a transition of the fracture propagation mode from synchronous radial–circumferential growth to circumferentially dominated propagation.

Once a complete fracture surface has been formed, unfilled regions within the fracture act as low-resistance flow pathways. The fracturing fluid then preferentially fills the fracture plane and progressively rebuilds fluid energy at the fracture tip, ultimately facilitating the initiation of the next fracture nucleation cycle.

3.1.3. Field-core evidence

Although the dynamic propagation of hydraulic fractures cannot be directly observed under field conditions, post-fracturing core analyzes provide important indirect evidence for stage-dependent fracture propagation. Fracture branching is commonly observed in core samples at locations distal to the perforations (Fig. 7), and the positions of these branches do not correspond to the perforation geometry. This observation indicates that fracture propagation does not proceed as a continuously advancing process. Instead, fractures undergo localized arrest followed by re-nucleation during growth, consistent with the experimentally identified cyclic, stage-dependent propagation behavior.

3.2. Stress-interaction-driven three-stage hydraulic fracture propagation and the formation of fracture swarms

The post-fracturing fracture morphologies of specimens #1 and #2 are summarized in Fig. 8. The experimental results indicate that in-plane inter-fracture interaction induces deflection of the affected fracture surface, resulting in the formation of a curved fracture geometry. By contrast, out-of-plane inter-fracture interaction preferentially promotes fracture branching, while the primary fracture surface remains relatively planar. Under strong interaction conditions (specimen #1), the fracture associated with wellbore 1, fracture II, which is subjected to in-plane interaction, exhibits a markedly higher degree of curvature. For fractures influenced by three-dimensional spatial interaction—specifically wellbore 2, fractures I and II—the number of branch fractures increases systematically with increasing well spacing, indicating enhanced fracture branching under stronger spatial interaction.

3.2.1. Stage I: multipoint fracture nucleation

During Stage I (multipoint fracture nucleation), fracture initiation is not confined to the tips of pre-fabricated fractures; instead, multiple fracture nuclei form nearly simultaneously. As shown in Fig. 9, during the early stages of propagation, fracture nucleation

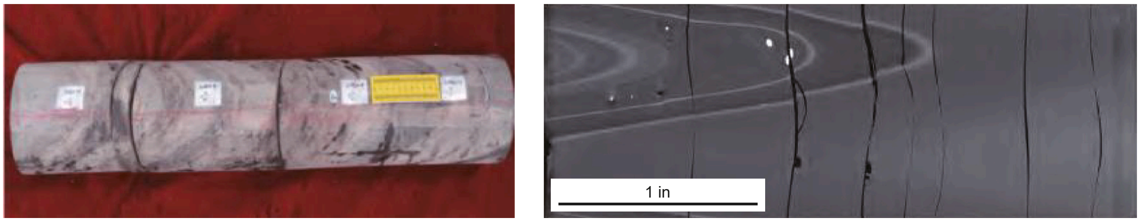

(a) Cores from Well Qing-41 **(b)** Cores from the HFTS-1

Fig. 7. Representative centimeter-scale distributions of hydraulic fractures observed in post-fracturing cores.

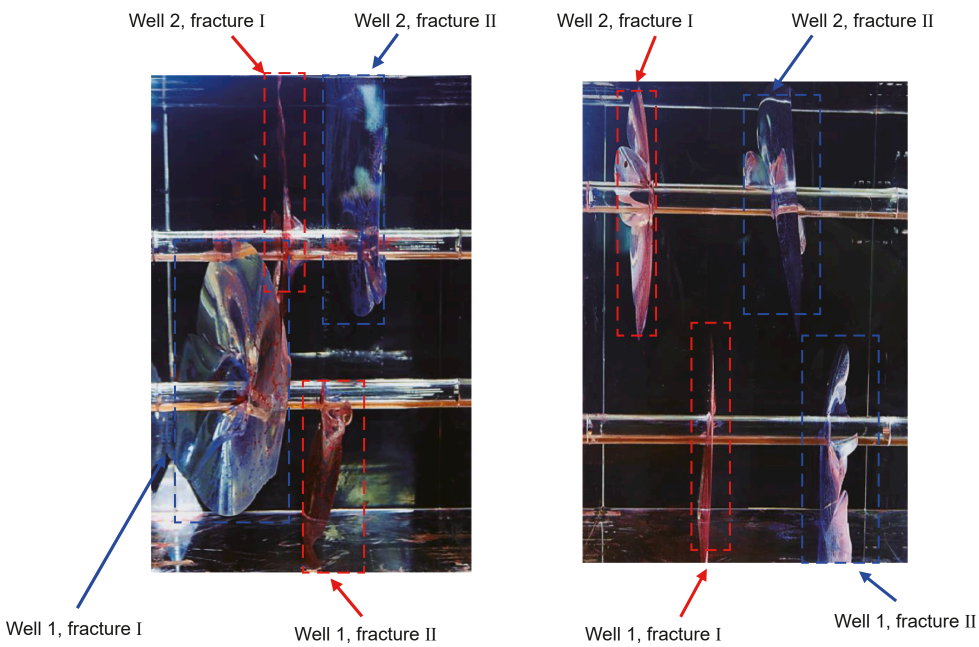

(a) Specimen #1 **(b)** Specimen #2

Fig. 8. Post-fracturing fracture morphologies under different inter-fracture interaction conditions.

commonly occurs at multiple locations near the advancing fracture front, rather than as a single, isolated event.

Fig. 9 further reveals that the characteristics of re-nucleated fracture branches differ depending on the mode of inter-fracture interaction. For fractures subjected to in-plane inter-fracture interaction, re-nucleated branch fractures form at an angle of approximately 70° relative to the primary fracture. Blue fluorescent tracer is observed within the branch fracture surfaces, indicating hydraulic connectivity between the branch and the primary fracture (Fig. 9(a)). In contrast, for fractures influenced by out-of-plane inter-fracture interaction, the re-nucleated branch fractures are oriented nearly parallel to the primary fracture, and no tracer is detected within the branch fractures. This observation indicates that these parallel branches are hydraulically isolated from the primary fracture.

During the fracture nucleation stage, stress interaction primarily operates by modifying the stress-field distribution in the vicinity of neighboring fracture tips, thereby promoting the formation of multiple fracture nuclei near newly generated tips. This behavior can be interpreted within the framework of a stress intensity factor (SIF) model, as described below (Eq. (2)):

$$K_{\mathrm{I}} = f(\sigma, r, r_0, m) \propto \frac{f}{r^m}\sqrt{\pi r_0} \tag{2}$$

where f denotes the applied pressure, r represents the distance from the fracture tip to a neighboring fracture, r_0 is the initial fracture length, and m is a geometric constant related to fracture configuration. The induced stress reaches its maximum along the extension line of the primary fracture, resulting in a reduction of the stress intensity factor by approximately 30%–40%, taken as 35% in this study. Under these conditions, the fracture preferentially deflects by an angle of approximately 70°, giving rise to branch formation. The branch fractures remain hydraulically connected to the primary fracture, as evidenced by the penetration of blue fluorescent tracer, ultimately forming a characteristic Y-shaped fracture geometry.

For out-of-plane stress interaction (Fig. 9(b)), the induced stress field extends over a broader spatial range in directions perpendicular to the primary fracture. As a result, fractures form near the pre-fabricated fracture and are oriented nearly parallel to the primary fracture but remain hydraulically disconnected, as evidenced by the absence of fluorescent tracer within the branch fractures. This observation indicates that the primary fracture and the parallel branch fractures are driven by distinct pressure sources rather than by direct hydraulic connectivity. Moreover, out-of-plane stress interaction generates a greater number of branch fractures than in-plane interaction, reflecting the larger spatial

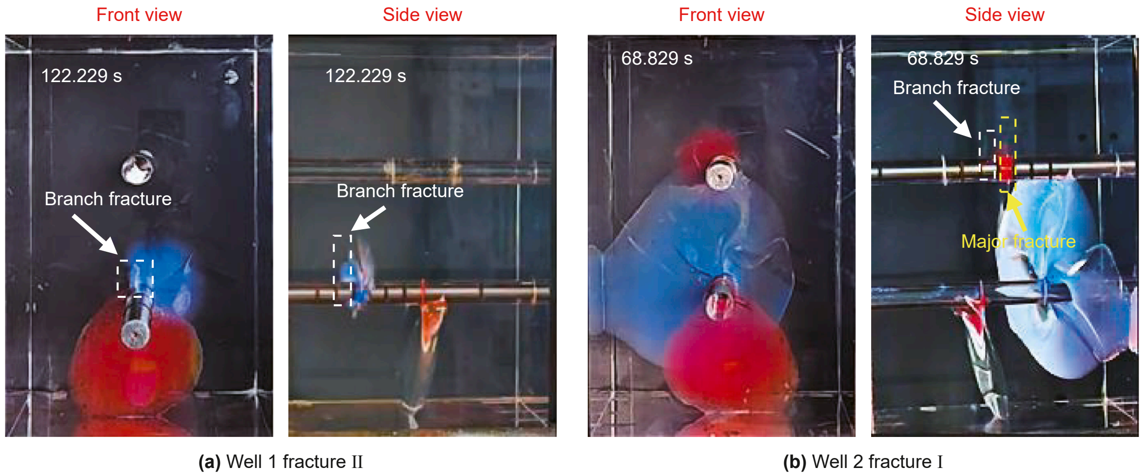

Fig. 9. Multipoint fracture nucleation under stress interaction in specimen #1.

extent over which the induced stress field influences fracture nucleation.

3.2.2. Stage II: fracture deflection and fluid energy competition

Once fractures enter the synchronous radial–circumferential propagation stage, the influence of inter-fracture interaction is expressed through the coupled effects of fracture deflection and fluid energy competition. At the onset of this stage, the primary fracture provides a wider and hydraulically more efficient flow pathway. Consequently, the injected fracturing fluid preferentially enters the primary fracture, driving a rapid increase in its fracture surface area, as illustrated in Fig. 10(a) (specimen #1, wellbore 2, fracture I). Under these conditions, branch fractures experience insufficient fluid energy supply and temporarily cease to propagate.

As fracture propagation proceeds toward more distal regions, frictional resistance to fluid flow within the primary fracture increases progressively. The branch fractures then gradually evolve into energetically favorable flow pathways, allowing sufficient fluid energy to be redistributed to them. As a result, these branch fractures enter the synchronous radial–circumferential propagation stage and resume active growth. In contrast, branch fractures that remain hydraulically disconnected from the primary fracture are unable to receive additional fluid energy and therefore fail to develop further, as shown in Fig. 10(b).

During the synchronous radial–circumferential propagation stage, fracture-path deflection is governed not only by stress interaction but also by fluid energy competition, which together determine the prevailing fracture propagation mode. Owing to differences in fracture geometry, aperture, and effective flow pathways, fluid energy is unevenly distributed among interacting fractures. This inter-fracture energy competition causes fracture nuclei associated with hydraulically favorable pathways to preferentially acquire fluid energy and transition into the synchronous propagation stage. The visualized experimental observations provide direct support for this mechanism. The fluid energy competition process can be quantitatively described by Eq. (3):

$$q_i \propto \frac{w_i{}^3}{\mu_{eff}} \frac{\partial p}{\partial s_i} \tag{3}$$

where q_i represents the fluid influx into branch fracture, w is the corresponding branch fracture aperture, μ_{eff} is the effective fluid viscosity, and $\frac{\partial p}{\partial s_i}$ denotes the pressure gradient along the flow path.

It is evident that the fluid influx into a branch fracture is positively correlated with both the branch fracture aperture and the imposed pressure gradient.

To further investigate the influence of fluid energy input on branch-fracture propagation, additional experiments were conducted in which the injection rate was increased by 50% to 45

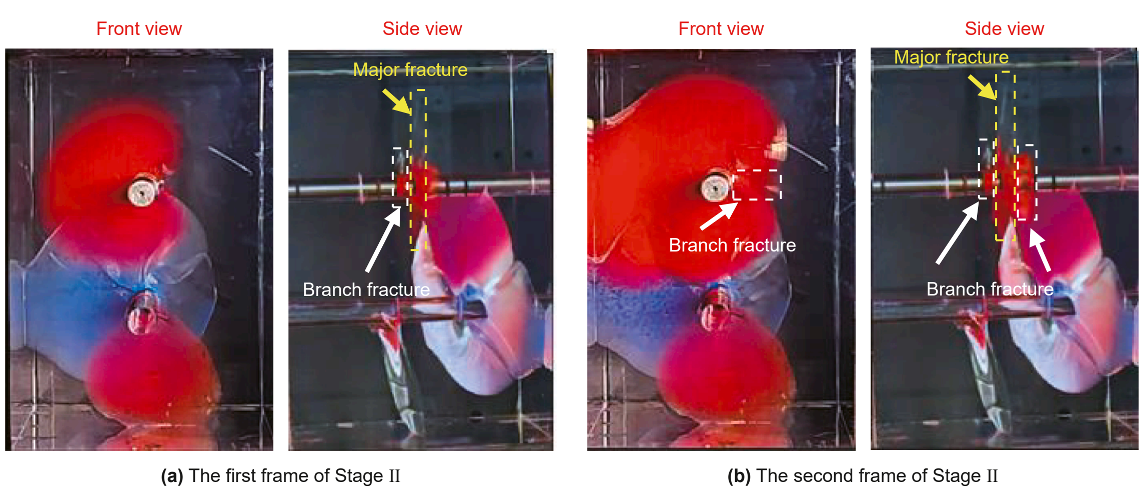

Fig. 10. Fracture propagation behavior during Stage II.

mL/min, while all other experimental conditions were held constant (specimen #3). Fig. 11 presents the dynamic behavior of fracture II in wellbore 1 of specimen #3 during the synchronous radial–circumferential propagation stage. The results demonstrate that, under substantially enhanced fluid energy input, both the primary fracture and its associated branch fractures enter the synchronous propagation stage simultaneously following irregular nucleation. This behavior arises because the increased fluid energy supply is sufficient to open both the primary and branch flow pathways at the onset of fracture nucleation, thereby enabling concurrent growth of the primary fracture and branch fractures.

The experimental results indicate that the synchronous radial–circumferential propagation stage fundamentally represents a process of fracture-path selection driven by fluid energy competition. According to lubrication theory (Eq. (1)), fluid flow within a fracture is governed by the pressure gradient and preferentially follows pathways with lower hydraulic resistance. Following the formation of fracture nuclei with associated branch fractures, three competing flow pathways coexist within the three-dimensional fracture nucleus: (i) radial flow toward the fracture-front tip, (ii) circumferential flow toward the lateral margins of the fracture nucleus, and (iii) diversion of fluid into branch fractures.

During the synchronous radial–circumferential propagation stage, the hydraulic resistance associated with pathways (i) and (ii) is comparable. Under these conditions, the aperture of branch fractures becomes the critical factor controlling fracture propagation behavior. At high injection rates, sufficient fluid energy is available to simultaneously supply both the primary fracture and branch fractures, enabling their concurrent radial–circumferential propagation. In contrast, at lower injection rates, the primary fracture—having already developed a larger aperture—offers a hydraulically more favorable pathway, whereas the smaller aperture of branch fractures results in increased frictional resistance. Consequently, fluid energy is preferentially channeled into the primary fracture, promoting its continued propagation while suppressing further growth of branch fractures.

3.2.3. Stage III: fracture-nucleus reactivation and step-like fracture formation

Taking fracture II in wellbore 1 of specimen #1 as an example (Fig. 12), once the fracture enters the circumferentially dominated propagation stage, the radial length of the single-wing fracture becomes sufficiently large that radial fluid flow experiences markedly increased hydraulic resistance. As a consequence, fluid transport preferentially shifts toward circumferential flow. Under these conditions, the previously suppressed fracture wing is re-energized by circumferentially transported fracturing fluid. Owing to its shorter radial flow distance, this wing exhibits pronounced reverse fluid flow, which in turn drives reverse extension of the previously inhibited fracture. This process reflects the reactivation of fracture nuclei during Stage III propagation.

A key distinction between circumferentially dominated reverse fracture extension and synchronous radial–circumferential propagation lies in the instability of the driving energy associated with circumferential flow. Experimental observations reveal that, at the tips of fracture surfaces on the previously suppressed side, characteristic shell-like and step-like fracture morphologies develop, analogous to those shown in Fig. 13.

We interpret these features as a characteristic manifestation of stress shadowing in controlling fracture morphology. When multiple fractures propagate synchronously within a confined spatial domain, the compressive stress zones generated between adjacent fractures exert a direct perturbation on fracture geometry. According to Eq. (4), the induced stress field associated with neighboring fractures significantly reduces the Mode I stress intensity factor of the primary fracture. In addition, asymmetry in the stress distribution introduces an additional shear component at the fracture tip. This combined stress state promotes fracture-tip deflection, thereby exerting a fundamental control on the resulting fracture morphology (Eq. (4)):

$$K_{\mathrm{I}} = K_{\mathrm{I}}^{(0)} + \Delta K_{\mathrm{I}}, \quad \Delta K_{\mathrm{I}} \propto \Delta\sigma_{\theta\theta}\sqrt{\pi a} \tag{4}$$

where K_{I} denotes the Mode I stress intensity factor; $\sigma_{\theta\theta}$ represents the circumferential stress perturbation induced by neighboring fractures; and a is the fracture half-length.

In combination with the maximum tangential stress criterion (Eq. (5)), fractures subjected to strong stress interaction exhibit a mixed Mode I–Mode II fracture behavior. During propagation, the fracture front alternates repeatedly between Mode I (tensile) and Mode II (shear) fracture mechanisms, ultimately imprinting characteristic step-like and shell-like features on the fracture surface. This mechanism provides a physical explanation for the rough fracture surfaces and pervasive step-like textures observed in field-derived core samples.

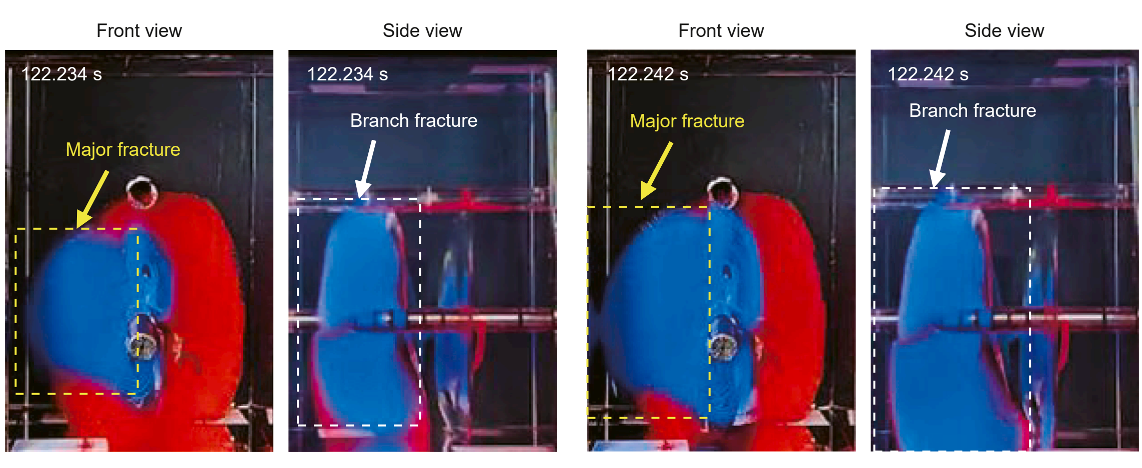

Fig. 11. Synchronous radial–circumferential propagation in specimen #3.

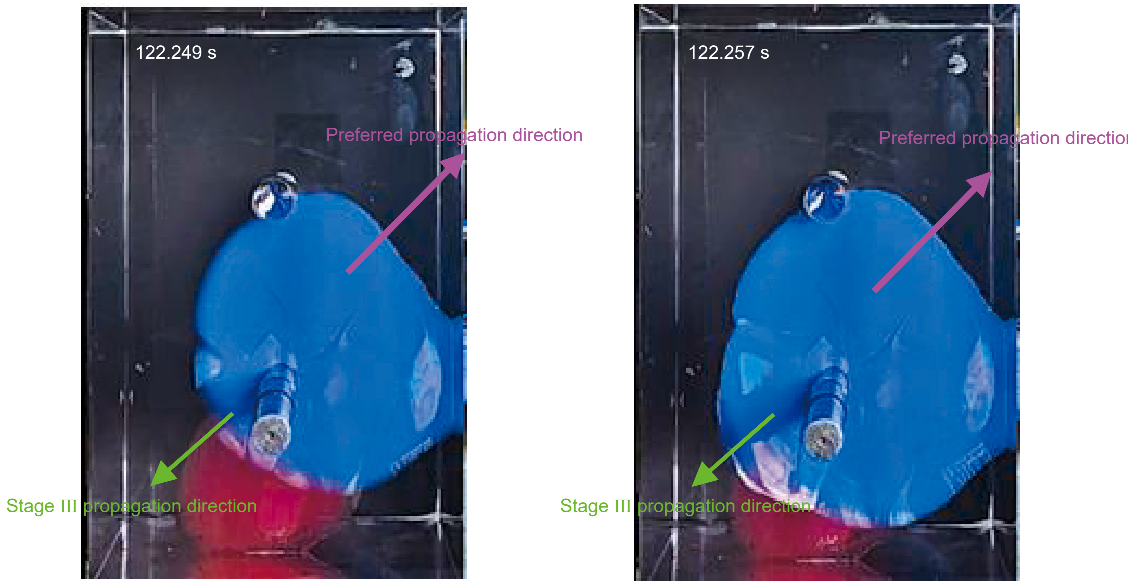

Fig. 12. Front-view dynamics of fracture propagation during the circumferentially dominated stage in specimen #1.

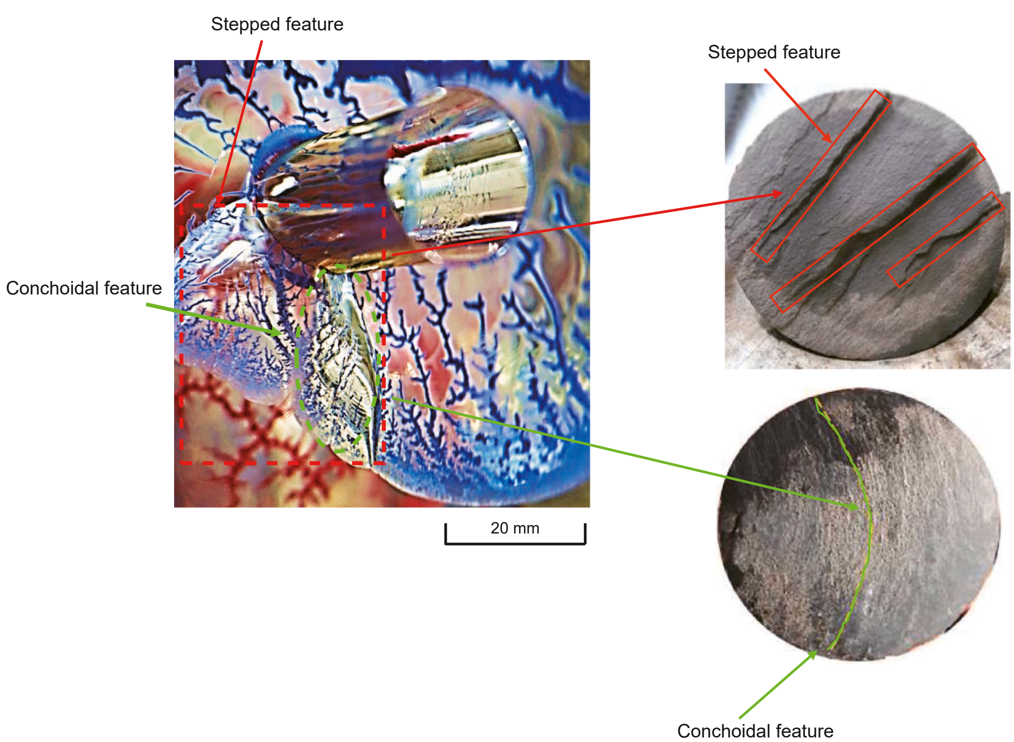

Fig. 13. Comparison of characteristic shell-like and step-like hydraulic fractures.

$$\theta = 2\tan^{-1}\left(\frac{K_{\mathrm{II}}}{K_{\mathrm{I}} + \sqrt{{K_{\mathrm{I}}}^2 + 8{K_{\mathrm{II}}}^2}}\right) \tag{5}$$

where K_{II} denotes the Mode II stress intensity factor.

4. Discussions

Post-fracturing cores from the Fuling shale gas field indicate that hydraulic fracture swarms exhibit a pronounced dependence on distance from the wellbore. Fracture density is highest in the near-wellbore zone (<35 m), decreases in the intermediate zone (35–100 m), and increases again in the far-field zone (>100 m) (Sun et al., 2025). This characteristic “dense–sparse–dense” pattern has been observed across multiple cored wells, suggesting that it is governed by systematic physical mechanisms rather than random variability.

4.1. Near-wellbore high-density fracture zone: sufficient fluid energy driving multi-branch simultaneous propagation

In the near-wellbore zone (<35 m), fluid pressure and energy supply are abundant. Wellhead pressures in typical Fuling wells are maintained at 50–70 MPa, and the net pressure within near-wellbore fractures can reach 30–40 MPa, far exceeding the critical pressure required for fracture propagation (approximately 10–15 MPa).

Experimental results indicate that under conditions of high energy supply, fractures first generate multiple nuclei during Stage I, after which both main fractures and branch fractures can simultaneously enter Stage II, forming complex multi-branch fracture swarms. Similarly, near-wellbore field fracture density is also 2.4–3.6 fractures/m, the highest in the entire well section. These artificial fractures exhibit complex combinations such as “Y-shaped” and “T-shaped” morphologies, which are consistent with multi-branch simultaneous propagation.

4.2. Intermediate low-density fracture zone: fluid competition propagation causing branch fracture stagnation

In the intermediate zone (35–100 m), fluid energy decays with distance. According to lubrication theory, for non-Newtonian fluids ($n \approx 0.6$), when distance increases from 30 m to 70 m, pressure gradient decreases by approximately 5.5 times, and fracture-tip energy decreases significantly.

Experiments demonstrate that under medium-to-low energy supply conditions, fluid competition mechanisms dominate fracture propagation behavior, and branch fractures stop propagating in early Stage II due to energy deficiency.

Fracture density in the intermediate zone (70 m) of Well A-J2 decreased to 2.78 fractures/m. Although fracture density in the intermediate zone (128 m) of Well A-J3 rebounded to 4.25 fractures/m, traceability analysis shows that fractures in this region are dominated by main fractures, with significantly reduced activated fractures and branch fractures. The formation of this sparse zone is essentially the result of fluid competition mechanisms selecting dominant fractures and suppressing secondary branches.

4.3. Far-field fracture density increased zone: stress field redistribution and fracture nucleus reactivation

In the far-field zone (>100 m), although fluid energy further decays, fracture density exhibits a rebound. Fuling coring data show that fracture density at 128 m in Well A-J3 reaches 4.25 fractures/m, and far-field density in Well A-J2 also shows an upward trend.

Experiments reveal the mechanism of this phenomenon: when main fractures extend toward distal ends, their radial flow resistance increases dramatically, and the relative flow resistance advantage of branch fractures re-emerges, causing previously stagnant branch fractures to reactivate and enter the simultaneous expansion stage. Meanwhile, because the perturbation of the surrounding stress field by the main fractures is fully developed, stress field redistribution occurs, forming new stress concentration zones along the flanks and fronts of main fractures and inducing the generation of new fracture nuclei.

5. Conclusions

Based on visualized hydraulic fracturing experiments and analysis of fracture propagation, we propose a staged formation mechanism for hydraulic fracture swarms and identify the associated controlling factors. The main conclusions are summarized as follows.

(1) Hydraulic fracture propagation follows a cyclic three-stage sequence that constitutes the fundamental mechanism underlying fracture swarm formation. The development of a single fracture proceeds through repeated cycles of local nucleation → simultaneous radial–circumferential propagation → circumferential-dominated propagation. Each cycle, lasting approximately 0.2–0.3 s at the experimental scale, generates a new fracture surface. Repetition of this sequence results in discontinuous fracture propagation and the formation of multiple closely spaced fractures, with spacings of 10–25 mm over centimeter-to decimeter-scale lengths. This behavior directly explains field observations in which the number of fractures preserved in cores exceeds the number of perforation clusters by a factor of four to eight.

(2) Fluid lag is the key physical mechanism triggering cyclic fracture propagation. When the fracture-front propagation velocity exceeds the fluid-supply velocity, unfilled lag zones develop near the fracture tip, causing the effective driving pressure to drop below the critical threshold. Consequently, the stress intensity factor decreases below the fracture toughness, leading to temporary stagnation of fracture propagation. The system then enters a re-pressurization stage, during which fluid progressively fills the lag zones and induces new fracture nuclei at locations of stress concentration, thereby initiating the next propagation cycle. This mechanism is expected to be universal under viscosity-dominated hydraulic fracturing conditions.

(3) Fracture swarm morphology is governed by the combined effects of stress interference and fluid competition, with their relative influences varying across different propagation stages. In Stage I, stress interference promotes multi-point fracture nucleation, leading to main-fracture–branch-fracture configurations. In Stage II, fluid competition controls branch activation: branches with larger apertures preferentially acquire fluid energy and continue propagating, whereas other branches stagnate. In Stage III, stress interference induces mixed Mode I–II fracture propagation on the suppressed side, resulting in the formation of stepped, shell-like fracture surfaces that are highly consistent with observations from field cores.

The above mechanisms provide a physical basis for understanding hydraulic fracture swarm formation and have important implications for optimizing fracturing stimulation design in unconventional oil and gas reservoirs.

CRediT authorship contribution statement

Yao-Yang Li: Writing – original draft, Methodology, Investigation, Data curation. **Guang-Qing Zhang:** Writing – review & editing, Project administration, Methodology, Funding acquisition. **Zhen-Yu Song:** Methodology, Investigation, Data curation.

Data availability statement

The data that supports the findings of this study are available from the corresponding author upon reasonable request.

Declaration of competing interest

The authors declare that they have no known competing financial interests or personal relationships that could have appeared to influence the work reported in this paper.

Acknowledgments

The authors wish to acknowledge the support of the National Natural Science Foundation of China (52434001).

References

Abe, A., Kim, T.W., Horne, R.N., 2021. Laboratory hydraulic stimulation experiments to investigate the interaction between newly formed and preexisting fractures. Int. J. Rock Mech. Min. Sci. 141, 104665. https://doi.org/10.1016/j.ijrmms.2021.104665.

AlTammar, M.J., Sharma, M.M., Manchanda, R., 2018. The effect of pore pressure on hydraulic fracture growth: An experimental study. Rock Mech. Rock Eng. 51, 2709–2732. https://doi.org/10.1007/s00603-018-1500-7.

Cao, W., Ma, Y., Meng, H., et al., 2025. Description and recognition of fractures in high-inclination coring well in Qingcheng shale oil hydraulic fracturing test site. China Petroleum Exploration 30 (2), 133–145. https://doi.org/10.3969/j.issn.1672-7703.2025.02.010.

Cochard, T., Svetlizky, I., Albertini, G., et al., 2024. Propagation of extended fractures by local nucleation and rapid transverse expansion of crack-front distortion. Nat. Phys. 20 (4), 660–665. https://doi.org/10.1038/s41567-023-02365-0.

Dontsov, E.V., Suarez-Rivera, R., 2020. Propagation of multiple hydraulic fractures in different regimes. Int. J. Rock Mech. Min. Sci. 128, 104270. https://doi.org/10.1016/j.ijrmms.2020.104270.

Gale, J.F., Elliott, S.J., Laubach, S.E., 2018. Hydraulic fractures in core from stimulated reservoirs: Core fracture description of HFTS slant core, Midland Basin, West Texas. In: SPE/AAPG/SEG Unconventional ResourcCes Technology Conference. https://doi.org/10.15530/URTEC-2018-2902624.

Gale, J., Elliott, S., Li, Z.J., et al., 2019. Natural fracture characterization in the Wolfcamp Formation at the Hydraulic Fracture Test Site (HFTS), Midland Basin, Texas. In: SPE/AAPG/SEG Unconventional Resources Technology Conference. https://doi.org/10.15530/URTEC-2019-644.

Gale, J.F.W., Elliott, S.J., Rysak, B.G., et al., 2021. Fracture description of the HFTS-2 slant core, Delaware Basin, West Texas. In: SPE/AAPG/SEG Unconventional Resources Technology Conference. https://doi.org/10.15530/URTEC-2021-5175.

Han, J., Zhao, Y., Li, H., Tan, J., et al., 2023. A comprehensive simulation study of Hydraulic Fracturing Test Site 2 (HFTS-2): Part II—Development optimization in the Delaware Basin using an integrated modeling workflow. In: SPE/AAPG/SEG Unconventional Resources Technology Conference. https://doi.org/10.15530/URTEC-2023-3851681.

Han, X., Yu, H., Wu, Y., et al., 2025. Experimental investigation on the counter-current imbibition distance and factors influencing the imbibition recovery of carbonated fracturing fluid. SPE J. 30 (3), 1474–1491. https://doi.org/10.2118/218205-PA.

He, J., Lin, C., Li, X., 2016. Experimental investigation of crack extension patterns in hydraulic fracturing with shale, sandstone and granite cores. Energies 9 (12), 1018. https://doi.org/10.3390/en9121018.

Hu, Y., Gan, Q., Hurst, A., et al., 2023. Investigation of coupled hydro-mechanical modelling of hydraulic fracture propagation and interaction with natural fractures. Int. J. Rock Mech. Min. Sci. 169, 105418. https://doi.org/10.1016/j.ijrmms.2023.105418.

Hubbert, M.K., Willis, D.G., 1957. Mechanics of hydraulic fracturing. Transactions of the AIME 210, 153–168. https://doi.org/10.2118/686-G.

Ishida, T., Chen, Q., Mizuta, Y., 1997. Effect of injected water on hydraulic fracturing deduced from acoustic emission monitoring. Pure Appl. Geophys. 150 (3), 627–646. https://doi.org/10.1007/s000240050096.

Lei, Q., Yun, X., Guan, B., et al., 2022. Progress and prospects of horizontal well fracturing technology for shale oil and gas reservoirs. Petrol. Explor. Dev. 49 (1), 191–199. https://doi.org/10.1016/S1876-3804(22)60015-6.

Li, X., Ji, H., Bian, T., et al., 2023. Characterization of hydraulic fractures in tight conglomerate reservoirs in Baikouquan Formation, Mabei slope. Xinjiang Petroleum Geology 44 (2), 178–183. https://doi.org/10.7657/XJPG20230207.

Maity, D., Ciezobka, J., Eisenlord, S., 2018. Assessment of in-situ proppant placement in SRV using through-fracture core sampling at HFTS. In: SPE/AAPG/SEG Unconventional Resources Technology Conference. https://doi.org/10.15530/URTEC-2018-2902364.

Manríquez, A.L., 2018. Stress behavior in the near fracture region between adjacent horizontal wells during multistage fracturing using a coupled stress-displacement to hydraulic diffusivity model. J. Petrol. Sci. Eng. 162, 822–834. https://doi.org/10.1016/j.petrol.2017.11.009.

Raterman, T.K., Farrell, H.E., Mora, S.O., et al., 2018. Sampling a stimulated rock volume: An Eagle Ford example. SPE Reservoir Eval. Eng. 21 (4), 927–941. https://doi.org/10.2118/191375-PA.

Sakha, M., Nejati, M., Driesner, T., 2023. On the initiation of hydraulic fractures in anisotropic rocks. Int. J. Rock Mech. Min. Sci. 169, 105429. https://doi.org/10.1016/j.ijrmms.2023.105429.

Sneddon, I.N., 1946. The distribution of stress in the neighbourhood of a crack in an elastic solid. Proc. R. Soc. London, Ser. A 187 (1009), 229–260. https://doi.org/10.1098/rspa.1946.0077.

Sobhaniaragh, B., Mansur, W.J., Peters, F.C., 2018. The role of stress interference in hydraulic fracturing of horizontal wells. Int. J. Rock Mech. Min. Sci. 106, 153–164. https://doi.org/10.1016/j.ijrmms.2018.04.024.

Sobhaniaragh, B., Haddad, M., Mansur, W.J., et al., 2019. Computational modelling of multi-stage hydraulic fractures under stress shadowing and intersecting with pre-existing natural fractures. Acta Mech. 230, 1037–1059. https://doi.org/10.1007/s00707-018-2335-8.

Song, J., Yu, H., Han, X., et al., 2025. Oil displacement and CO_2 storage mechanisms of impure CO_2 flooding in tight reservoirs: insights from microfluidic experiments and numerical simulations. Fuel 393, 134934. https://doi.org/10.1016/j.fuel.2025.134934.

Song, X., Liu, Y., Yang, X., et al., 2024. Quantifying the impact of geological and construction factors on hydraulic fracture dynamics in heterogeneous rock layers using the phase field method. Comput. Geotech. 169, 106223. https://doi.org/10.1016/j.compgeo.2024.106223.

Sun, H., Lu, Z., Liu, L., et al., 2025. Technology and understanding of post-fracturing coring in three-dimensional development zone of Fuling shale gas, Sichuan Basin, SW China. Petrol. Explor. Dev. 52 (3), 653–664. https://doi.org/10.11698/PED.20250054.

Sun, W., Zhang, G., Du, B., et al., 2024. Propagation of interfered hydraulic fractures by alternated radial-circumferential extensions and its impact on proppant distribution. Int. J. Rock Mech. Min. Sci. 181, 105838. https://doi.org/10.1016/j.ijrmms.2024.105838.

Tahir, S., Kindi, S., Ghorayeb, K., et al., 2019. A top-down view of field development plans, integrated reservoir performance and production sustainability assurance. In: Abu Dhabi International Petroleum Exhibition & Conference. https://doi.org/10.2118/197379-MS.

Talebi, S., Boone, T.J., 1998. Source parameters of injection-induced microseismicity. Pure Appl. Geophys. 153 (1), 113–130. https://doi.org/10.1007/s000240050187.

Tan, P., Kao, J., Cheng, F., et al., 2022. A review on hydraulic fracture height growth for layered formation. Geotech. Geol. Eng. 40 (8), 4057–4067. https://doi.org/10.1007/s10706-022-02138-1.

Urbancic, T.I., Shumila, V., Rutledge, J.T., et al., 1999. Determining hydraulic fracture behavior using microseismicity. In: The 37th U.S. Symposium on Rock Mechanics.

Wang, S., Tan, Y., Sangnimnuan, A., et al., 2019. Learnings from the Hydraulic Fracturing Test Site (HFTS) #1, Midland Basin, West Texas—A geomechanics perspective. In: SPE/AAPG/SEG Unconventional Resources Technology Conference. https://doi.org/10.15530/URTEC-2019-1570.

Wicker, J., Courtier, J., Campbell, T., et al., 2018. Using stage level microseismic analysis to correlate and ground truth cored hydraulic fractures. In: SPE/AAPG/SEG Unconventional Resources Technology Conference. https://doi.org/10.15530/URTEC-2018-2937221.

Xing, Y., Zhang, G., Wan, B., et al., 2019. Subcritical fracturing of sandstone characterized by the acoustic emission energy. Rock Mech. Rock Eng. 52, 2459–2469. https://doi.org/10.1007/s00603-018-1724-6.

Zhang, K., Mu, L., Qi, Y., et al., 2024. Overview and practical understanding of the construction of shale oil hydraulic fracture field labs in the Ordos Basin. Drill. Prod. Technol. 47 (6), 16–27. https://doi.org/10.3969/J.ISSN.1006-768X.2024.06.03.